Characterization of Microwave Radiometers and Study of Human Body Radiation by Means of State Space Reconstruction Algorithms

Sergey V. Kapranov[1], Guennadi A. Kouzaev[1] and Vladimir V. Tchernyi (Cherny)[2]

[1]*Norwegian University of Science and Technology (NTNU),*
O.S. Bragstads Plass 2B, 7491 Trondheim, Norway
[2]*Modern Science Institute, SAIBR, Osennii Blvd. 20-2-702, 121614 Moscow, Russia*
sergey.kapranov@iet.ntnu.no, guennadi.kouzaev@iet.ntnu.no, chernyv@list.ru

Abstract

This paper presents a detailed study of human body microwave radiation by methods of stochastic dynamics. Weak electromagnetic signals are received by a Dicke radiometer and their characteristics are investigated by statistical methods to exclude possible artifacts. The signals' deterministic content is detected by several methods of stochastic dynamics, and multi-attractors in the radiometric signals are observed. A novel method of finding the Hausdorff dimensions in the signals is proposed. The number of attractors and characteristics of their dimensions in each signal is found by means of the cluster analysis technique. These attractor dimensions of radiation of human bodies are compared with those of the background and radiometer noises, and the differences between these characteristics are noticed. Several hypotheses on the origins of this new interesting finding, including the physiological reasons, are proposed.

Keywords: *radiometer, time-delay state space reconstruction, attractor, fractal dimension, cluster analysis*

1. Introduction

Microwave radiometry (MR) is the registration of the electromagnetic (EM) thermally-caused radiation of objects in natural conditions. The power of microwave radiation from an object is proportional to its absolute temperature, so the signal can be recalculated in temperature units (*the brightness temperature*). Usually, the power of thermal signals is below the noise level of conventional receivers, and a special kind of them, radiometers, is designed for reliable signal registration. The material and its spatial structure influence the radiation, allowing remote sensing of natural or artificial objects to estimate their temperature, spatial shapes, and inner material structure [1-4].

The detection of the cosmic microwave background radiation in the 60-s [5] was the first spectacular success of MR, and it remains nowadays the subject of extensive MR investigations [6]. Many applications of MR are in medicine, as this method allows obtaining the thermal images from the inside of body in contrast to the infrared imaging [4, 7-11]. Now some developments are within security applications, and several radiometer vision systems have been developed for detecting weaponry hidden beneath the clothing without additional illumination [12-15].

Several practically used types of radiometers are known, and one of them is based on the first design invented by R. H. Dicke [16]. It exploits an idea of periodical switching the receiver from antenna to the equivalent noise source which has temperature equal to that of the receiver. The radiometer eliminates the thermal noise of the hardware by

means of periodical deduction of this noise from the input signal. A square-law detector is used to produce an output signal which is proportional to the input power. Then it is integrated over a rather long period to smooth the fluctuations, digitized by an analog-to-digital (A/D) converter, and registered as a time series in the memory of a computer.

In real conditions, the radiometers register the sum of the brightness temperature and the temperature of background EM noise in the frequency band concerned. The influence of the background radiation, referred in literature on MR to as the *radio frequency interference* (RFI), is considered as an adverse effect, especially at low radiances of objects under investigation. A variety of special techniques were proposed to reduce this interference [17-19].

None of radiometers is free of residual time-dependent hardware noise if practically-usable integration times are concerned. As a rule, the radiometer output signals show rather complicated dynamics, as the thermal and digital noise and the incoming thermal signals are nonlinearly mixed with each other in hardware. An account of basic spectral components of the noise in the microwave radiometric measurements is made in [20].

The resolution deterioration by the radiometer hardware noise can be partly reduced by instrumentation modification and application of special numerical procedures instead of expensive cooling of radiometers. Similarly, the undesirable influences of the RFI can be numerically reduced by appropriate processing of the output signals. To develop the algorithms for the improvement of the radiometer sensitivity and the RFI mitigation, the characterization of radiometers is essential. One of the possible approaches exploiting state-space reconstruction algorithms is considered in this work.

Unlike the factor analysis applied in the radiometric signal processing [3], the signal state-space reconstruction allows finding dimensions of the phase space in which the time-dependent signal is embedded, rather than establishing a specific relationship between the signal and the independent variables of this phase space. The first applications of this technique in processing microwave signals date back to the late 80-s [21]. In those experiments, strange attractors of different dimensions were discovered in the signals scattered by various natural surfaces. Later, these fractal structures were also found in microwave signals coming from the troposphere.

A state-space reconstruction method [22] was first applied to the human body microwave radiation in [23]. The results showed essential difference in some characteristics of the signals from each other and from those of white noise. In this paper, we present a more detailed study which allows finding and classing the deterministic noise nature by comparing the calculated parameters of signals, registered by the same one-channel Dicke-type radiometer as in [23], from eleven individuals, the reference 50-Ohm load, and the environment.

A modified phase-space reconstruction algorithm, developed and implemented in this study, is applied to each of these chaotic signals to find the characteristics and origins of the deterministic chaos. This is important, firstly, for the future development of efficient filtering algorithms for the elimination of the noise caused by the radiometer hardware to further improve the radiometer sensitivity. Also, this technique can reveal the deterministic chaos in the background EM radiation and facilitate the RFI mitigation in MR. Finally, it is potentially helpful for the radiometric detection of human presence if patterns of the deterministic noise originating from the human body radiation prove to differ from those associated with other sources.

Section 2 of this paper is devoted to some essential introductory material to the state-space reconstruction algorithm and to methods of calculation of the fractal dimensions. Also, a modification of one calculation method is proposed there. In Section 3,

application of these techniques to a multi-attractor system is shown. Section 4 is focused on a detailed description of the algorithm of calculating fractal dimensions in the radiometric multi-attractor signal. In Section 5, the experimentation and implementation of the data-processing algorithm with emphasis on one particular data set are described. The results of application of this algorithm are analyzed in Section 6. Section 7 concludes the study.

2. Techniques of Calculation of the Attractor Dimension

Typically, the nonlinear time-dependent processes can be chaotic due to dynamic instability, but the latent determinism can still be detected using the state-space reconstruction algorithms, *e.g.*, the technique proposed in [22]. These methods allow to consider a time series in an extended phase space and to find an attracting subset of this space (*an attractor*), around which the trajectories are concentrated and where they display oscillations of a certain type. If the deterministic chaos exists in a process in question, these procedures enable calculating the fractal dimension of the stochastic system's attractor (*the strange attractor*). The nearest integer above the attractor dimension indicates the minimal number of variables which fully describe the stochastic dynamics of the nonlinear deterministic process.

Consider a time series of N samples $s(t)$ registered by the radiometer. It is constituted by a number of processes incorporated in components of vectors $\mathbf{X}(t)$ which are unknown due to the complexity of the source dynamics. The idea of the algorithm is to obtain a minimal set of independent or orthogonal components of $\mathbf{X}(t)$. The state-space reconstruction procedure consists in constructing an m-dimensional vector time series $\mathbf{X}(t)$ from the initial series $s(t)$.

To find these vectors, a technique based on a rigorous proof [24] is used. It replaces the original time series $s(t)$ by its $(m–1)$ time lags τ, which constitute the vector time series in an m-dimensional state space [29-31, 36-39, 41-48, 50-55]:

$$\{\mathbf{X}_i\} \equiv \{\mathbf{X}(t_i)\} = \left\{\overline{\left(s(t_i), s(t_i+\tau), ..., s\left[t_i+(m-1)\tau\right]\right)}\right\} \tag{1}$$

where $i=1,2,\ldots, N-\lceil (m-1)\tau/\Delta t \rceil$, Δt is the constant time step in the original scalar time series, and N is the number of points in it. This vector series is further processed to yield the attractor dimension estimates. The reconstructed-space dimension m is referred to as the embedding dimension.

The choice of the time delay τ is an important issue since the correct state-space reconstruction requires that the vector components be decorrelated from each other. The simplest solution of this problem is the construction of an autocorrelation function with the subsequent finding of the coordinate of its first zero [25-28]. However, this function measures the linear dependence among the points, and it may be inappropriate for the nonlinear analysis. It is proposed in [29] that τ should be found as the local minimum of mutual information among the successive points. Another suggestion was made to take $\tau=T/m$ where T is the period of the dominant peak in the spectrum of the signal [26].

Among several types of attractor dimensions, two measures can be selected: the correlation dimension d_c and the Hausdorff dimension d_H. In general, the latter is the upper limit of the fractal dimension and the former always being smaller or equal to it [22]:

$$d_c \le d_H. \tag{2}$$

For finding d_c, the calculation of the correlation integral $C(r)$ is required [22]. This correlation integral is shown to be a power-law function of the correlation dimension [22, 27] which is determined according to the following formula, once the fractal is completely embedded in the state space:

$$d_c = \lim_{r \to 0} \left[\ln C(r) / \ln r \right]. \tag{5}$$

The Hausdorff dimension dealing with the infinite number of points is usually expressed as the box-counting dimension for a finite set of vectors. In the box-counting procedure, one assesses how many m-dimensional hypercubes with edge ε are sufficient to cover all points specified by vectors $\mathbf{X}$ in the state space. Sometimes, it is more convenient to count the hyperspheres of radius ε instead of the hyperboxes [27].

Let $n(\varepsilon)$ be the minimum number of the hyperspheres of radius ε which is necessary to cover all the mentioned points of the m-dimensional phase space. This number of the hyperspheres is a reciprocal power-law function of the Hausdorff dimension, and it can be found as the number of unique integer part combinations of $\mathbf{X}/\varepsilon$ [30]. Then, under the stipulation that the fractal is completely embedded in the phase space, the Hausdorff dimension in its box-counting variant is [27, 30]

$$d_H = \lim_{\varepsilon \to 0} \left[\ln n(\varepsilon) / \ln(1/\varepsilon) \right]. \tag{6}$$

According to (5) and (6), the fractal dimensions are found as the slopes of straight lines plotted by the least-squares method in the coordinates $\log C(r) - \log r$ and $\log n(\varepsilon) - \log(1/\varepsilon)$ in the region of small r and ε, respectively.

The above-mentioned dimensions can be united in one definition [27, 31]. Let an interval of the phase space be divided into n subintervals. The probability of the trajectory visiting a particular i-th subinterval is defined as p_i. Then, the definitions of dimensions (5) and (6) can be combined into a generalized dimension of order q:

$$d^{(q)} = \frac{1}{q-1} \lim_{\varepsilon \to 0} \left(\ln \sum_{i=1}^{n} p_i^q \Big/ \ln \varepsilon \right). \tag{7}$$

It can be shown [27, 31] that the generalized dimension takes the form of the box-counting dimension (6) when q=0 and it turns into the correlation dimension (5) when q=2. The equality $d_c = d_H$ in (2) is fulfilled only when trajectory points have uniform distribution over the phase space interval (p_i=1/n), in accordance with (7).

It is possible to find the Hausdorff dimension using another procedure somewhat different from counting the minimal number of hyperspheres covering $\mathbf{X}$. Consider a set of vector differences $\mathbf{X}_i - \mathbf{X}_j$. Similar to finding whether a phase space vector belongs to a certain hypersphere [30], the number G_i of unique combinations of integer parts of $(\mathbf{X}_i - \mathbf{X}_j)/\varepsilon$ determines the minimum number of hyperspheres sufficient to cover these differences. If $\mathbf{X}_i$ is a reference vector and $\mathbf{X}_j$ vectors are "clustered" in groups smaller than ε then G_i determines how many ε-sized groups exist with respect to $\mathbf{X}_i$. Hence, the average number of vectors in a hypersphere associated with ith vector is n/G_i.

According to the interpretation set forth in [48], the correlation integral ensues from (7) with q=2:

$$C(\varepsilon)=\sum_{i=1}^{n} p_i^2=\langle p_i\rangle=\tfrac{1}{n}\sum_{i=1}^{n} p_i\approx\tfrac{1}{n}\sum_{i=1}^{n}\frac{\text{average number of vectors in } i\text{th hypersphere}}{n}$$
$$=\tfrac{1}{n}\sum_{i=1}^{n} n/G_i=\langle n/G_i\rangle. \tag{8}$$

Then,

$$1/p_i\approx G_i/n. \tag{9}$$

Hence, the Hausdorff dimension can be derived from (7) with q=0 and finite n as

$$d_{\mathrm{H}}=-\lim_{\varepsilon\to 0}\frac{\ln\sum_{i=1}^{n} p_i\,(1/p_i)}{\ln\varepsilon}=-\lim_{\varepsilon\to 0}\frac{\ln\langle G_i/n\rangle}{\ln\varepsilon}=-\lim_{\varepsilon\to 0}\frac{\ln\langle G_i\rangle-\ln n}{\ln\varepsilon}\approx-\lim_{\varepsilon\to 0}\frac{\ln\langle G_i\rangle}{\ln\varepsilon}. \tag{10}$$

The box-counting dimension defined according to (6) will be referred in this work to as the Method-1 Hausdorff dimension ($d_{\mathrm{H},1}$) and that found from (10) will be termed the Method-2 Hausdorff dimension ($d_{\mathrm{H},2}$).

The range of r in which the correlation dimension can be determined is limited by the values of the correlation integral varying theoretically from $2/n^2$ to 1 [27]. However, $C(r)$, $n(\varepsilon)$, and $\langle G\rangle(\varepsilon)$ are meaningful when r or ε are in the range between the smallest and the largest absolute vector differences. In practice, the ranges of these arguments used for finding the dimensions depend on n, m, and range of data set variation. An empirical method of locating the lower boundary of ε and r used in determining the dimensions of an attractor is described below in Sect. 4.

To verify the codes, the Lorenz equations [32] have been integrated numerically in Matlab using the fourth-order Runge-Kutta algorithm with Δt =0.005, N =2048, and the parameters of the equations as in [25]. The first zero of the time-dependent autocorrelation function is found at τ=0.79. It allows calculating the vectors $\mathbf{X}(t)$, the correlation integral $C(r)$, and the numbers of hyperspheres $n(\varepsilon)$ and $\langle G\rangle(\varepsilon)$.

All the three dimensions of the Lorenz attractor are calculated for m=2, 3,…, 10, and d_{c}, $d_{\mathrm{H},1}$, and $d_{\mathrm{H},2}$ are found as the saturation levels of the dimensional estimate curves. Takens suggested [24] that a functional series dimension converges when

$$2m+1\geq d. \tag{11}$$

The saturation of the correlation dimension plot is indeed attained when the condition (11) is satisfied. The Method-2 box-counting dimension is slightly slower in the convergence, and the Method-1 box-counting dimension plot comes most sluggishly to the saturation, converging only at m=8. The slower convergence of the Method-2 and Method-1 box-counting dimension plots is accounted for by the relatively small number of data samples which is most crucial for finding the Hausdorff dimension [27].

In practice, due to numerical errors and certain arbitrariness of choosing the linearity interval in the log-log plots, the dimensional estimates above the convergence fluctuate around the mean value. The uncertainty of calculating the dimensions is represented by the standard deviation. The Lorenz attractor convergence has yielded the correlation dimension d_{c}=2.09 with the standard deviation 0.06 and the Hausdorff dimensions $d_{\mathrm{H},1}$=$d_{\mathrm{H},2}$=2.05 with the standard deviations 0.02. The Lorenz attractor dimensions are found in agreement with the results obtained by other authors [22, 25, 30].

Difficulties in calculating the correlation dimensions can be encountered for signals contaminated by the Gaussian noise which produces slopes equal to the embedding dimension in the small-r areas [27, 25]. The box-counting dimension appears to be much less sensitive to the Gaussian noise, according to [25].

The number of data points is critical for measuring the fractal dimension. According to different approaches, a 5% error in the dimension estimation probability is attained for a data set with a minimum number of points 5^d [27] or $10^{2+0.4d}$ [26]. The methods which can essentially reduce the minimum number of data points were reported, e.g. in [33]. Takens' theory of best estimator results in the 5% error level for as few as 1.25^d data points [27].

Thus, very extensive data sets are required to obtain high attractor dimensions with good accuracy. However, the MR samplings are typically slow, and it is virtually impossible to accumulate the time series with more than several thousand points. Moreover, the phase-space reconstruction duration varies as N^2, so processing of larger data sets will consume increasingly longer times. Therefore, some tradeoff between the dimension accuracy and the time limitation should be reached. In this work, we do not in any way attempt to estimate the optimum size of the data sets, but it is demonstrated that, taking advantage of the developed algorithm, as few as 121 points are sufficient for discerning the signal from individuals in some cases.

3. Calculation of Dimensions in Multi-attractor Systems

The above methods focus on finding a single attractor dimension from the time-delay reconstruction of a phase space. However, the time-dependent signal radiated by human body can contain origins of more than one fractal attracting set. The resulting signal will incorporate traces of these fractals on different size scales. It will be referred to as the *multi-attractor* signal. In the strict sense, this signal contains only one attractor with the corresponding dimensions defined according to (5)-(7), but it is treated as if it were comprised of several attractors isolated in delimited size ranges of the phase space. In other words, the multi-attractors can have more than one fixed-order dimension in different regions of the size parameter variation.

The introduced concept of a multi-attractor should not be confused with the generally-accepted term *multiple fractal*, or *multifractal*. Multiple fractals emerge when probability of a trajectory visiting different areas of the phase space is not uniform. Multifractals are well-defined in dynamics of a number of mathematical and physical systems (see, for example, [27, 34, 35] and references therein). The singularity scaling formalism introduced in [34] yields analytical spectra of generalized dimensions (7) versus q varying from $-\infty$ to $+\infty$ for a number of multifractal sets.

The mathematically strict concept of the multifractal generalized dimension spectrum could be helpful in analyzing the radiometric signals; however, it is inapplicable if the probability distribution in the reconstructed phase space is unknown, as in our case. The procedure of calculating these probabilities utilized in [35, 36] solves this problem but complicates the dimension analysis to a considerable extent. Instead, we propose a facile multi-attractor approach to estimating the fixed-order dimension patterns of the radiometric signals. As shown below, these patterns turn out to be imprecise, but they are easily obtained and can in principle apply for distinguishing signals of individuals from those of the load and the background.

To understand the origination of several local dimension measures in the correlation integral of a radiated signal, consider two cases of overlapping and non-overlapping fractal sets with different dimensions. If one fractal with the correlation dimension d_1

overlaps with another one with the correlation dimension d_2 starting from r_0, then their contribution to the logarithm of the correlation integral at distance $r>r_0$ is

$$\ln C_o = \ln c_2 + d_2 \ln r + \ln\left[1+\left(c_1/c_2\right)r^{d_1-d_2} - \left(r_0/r\right)^{d_2}\right] \tag{12}$$

where c_1 and c_2 are the proportionality factors.

The last term in the right-hand part of (12) is negligible if $1<d_1<d_2$ and $c_1 \sim c_2$. Then $\ln C_o$ has slope d_2 for $r>>r_0$ and slope d_1 at distances below r_0. This case is represented by the correlation integral curves of Figure 1(a) with the sharp bends between their linear sections corresponding to r_0-values. On the other hand, (12) can be rewritten as

$$\ln C_o = \ln c_1 + d_1 \ln r + \ln\left[1+\left(c_2/c_1\right)\left(r^{d_2} - r_0^{d_2}\right)\Big/ r^{d_1}\right] \tag{13}$$

in which the last term can be neglected if $1<d_2<d_1$. In this case, the correlation integral has slope d_1 over the whole range of distances except a narrow area near r_0.

In the case of two non-overlapping fractals with the same parameters as above and the boundary lying at r_0, the logarithm of the correlation integral is

$$\ln C_{no} = \ln c_2 + d_2 \ln r + \ln\left(1+\left[c_1/c_2\right]\left(r_0^{d_1}/r^{d_2}\right) - \left[r_0/r\right]^{d_2}\right) \tag{14}$$

in which the last term is of the order of zero provided $c_1 \sim c_2$. Then ln C_{no} has slope d_2 at distances above r_0 and slope d_1 at distances below r_0.

Thus, finding local slopes at the correlation integral curve against r in log-log coordinates allows identifying individual fractal dimensions of a multi-attractor data set when the condition of the size parameter tending to zero is relaxed. An ideal picture of correlation integral plots describing two overlapping fractals is shown in Figure 1(a). The horizontal lines denote the slope-estimation areas. Unlike an ideal single-fractal plot, two distinct local slopes in these plots are discernable. As shown in Figure 1(b) by the dashed lines, the lower dimension converges close to $d_{1,c} = 0.97$ and the higher one converges around $d_{2,c} = 1.88$.

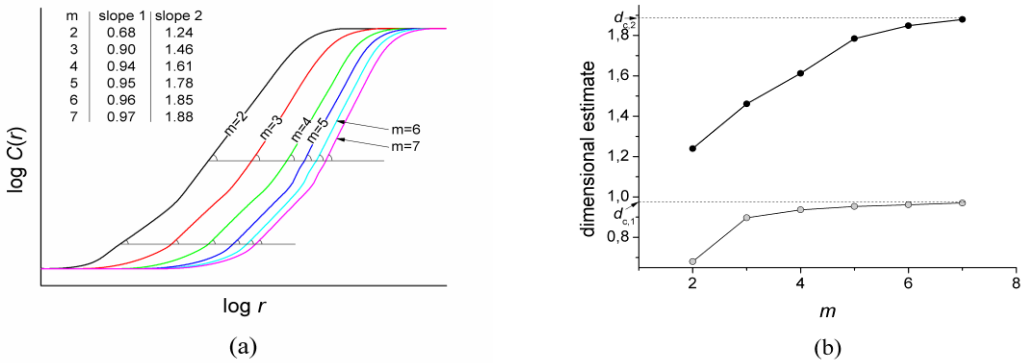

Figure 1. (a) Idealized Bi-attractor Correlation Integrals vs. the Size Parameter *r* in Logarithmic Coordinates; (b) The Slopes (dimensional estimates) vs. the Embedding Dimension

To obtain the spectrum of multi-attractor dimensions of the human-radiated signals, analysis based on extracting local slopes of $C(r)$ and $\langle G\rangle(\varepsilon)$ in log-log coordinates over the whole region of r- and ε-variation has been performed. It is reported below in detail.

4. Data Processing Method for Multi-attractor Signals

The data fewness and diversity of fractal structures concealed in the body-emitted signal complicates the analysis and interpretation of the reconstructed time series. Moreover, the device itself and the background noise generate such structures hidden in the signal. Therefore, it is important to develop an algorithm which could allow reliably obtaining spectra of the multi-attractor dimensions in the signals of the individuals, load, and background. Comparing them, one can then figure out peculiarities of the signals and judge the possibility of distinguishing between them.

As a starting point, one can see in Figure 1(a) that the linear sections corresponding to certain dimensional estimates are separated from each other by bends, *i.e.*, the sections with considerable curvature. This fact is used further in the slope-finding procedure.

The following algorithm for finding local slopes of the correlation integral and number of spheres in the logarithmic coordinates for a constant embedding dimension has been used. The lower limit of both the correlation integral and hyper-sphere-counting slopes is determined as the boundary where the curvature of the line connecting adjacent points falls to near-zero values. The curvature of a function $y(x)$ is

$$\kappa = \left[1+\left(dy/dx\right)^2\right]^{-3/2} d^2y \Big/ dx^2 . \tag{15}$$

The assumption that $y_1(x_1)\equiv\log C(r)$ and $y_2(x_2)\equiv\log N(\varepsilon)$ are continuous functions of $x_1\equiv\log r$ and $x_2\equiv\log(1/\varepsilon)$, respectively, allows applying this formula to the log-log plots. By analogy drawn to discrete data series, one can replace first and second derivatives in (15) by finite increment ratios. In Figure 3, examples of such plots for the person S data and m=15 are presented. The area of the linear sections is bounded on the side of large negative values of log r and small negative values of log $(1/\varepsilon)$ by the finite resolution of the phase space portraits. At the opposite sides of the arguments, it is restricted by the finite area of the fractal in the phase space.

Consider first the case of a single fractal dimension. The dimension determination requires, on the one hand, that the slopes should be with high degree of linearity. On the other hand, to meet the size parameter smallness conditions in (5) and (10), the linearity region must be as close to the lower argument boundaries as possible. For that reason, the onset of linearity in correlation integral plots will be arbitrarily defined as abscissa of the first point of two consecutive ones with absolute mean curvature less than 0.2 and standard deviation less than 0.1 following a point which does not satisfy these criteria. It is at large negative values of log r. On the contrary, the lower limit of the linearity area in hypersphere-counting plots is located at large values of log $(1/\varepsilon)$. It is defined similarly, but the absolute mean curvature of two consecutive points is assumed to be less than 0.5 and the standard deviation is less than 0.25. It is seen in Figure 3 that near-zero curvatures defined in such a way are attained at log r = –1.70 for the correlation integral plot and at log $(1/\varepsilon)$ = –1.50 for the hypersphere-counting plot at m=15. These coordinates are considered as the lower boundaries of detectable slopes and are marked with bold arrows. The upper limits could be defined in exactly the same way starting from the opposite side of the plots, but there is usually no need in doing

this because of existence of distinct breaks in the slopes typically encountered over the linearity regions. These breaks are characterized by large curvature and should be regarded as the end of the slope calculation area for a single fractal.

In the case of multi-attractors, these breaks demarcate the boundary between the areas of calculating two different dimensions, as it follows from (12) and (13). Because a limited number of data points can distort the linearity to a considerable extent, one has to develop a special algorithm of finding limit curvatures below which the corresponding points in the log-log plot section are still described by a single line and above which the slope is assumed to change. Furthermore, close values of individual slopes thus found, though different due to the statistical straggling, may be assigned to one and the same fractal dimension. It is therefore necessary to distinguish the groups encompassing the closely set slopes. The algorithms of ascertaining which points in the log-log plots are described by a single line, and discriminating the slope groups are set forth in 4.1 and 4.2, and an example of the algorithm application is given in Section 5.

4.1. Exploiting Limit Curvature Determination in the Detection of Slopes

First, we cancel the condition of lower boundary defined above for a single fractal. Instead, we arbitrarily fix the minimum value of slopes stipulating that they must be greater than unity. Starting from both ends towards the linearity region, linear fits of every three points in a row in the log-log plots are obtained. The first three points from both sides fitted by a line with slope higher than unity designate the onset of the working area. Other points are discarded.

In fact, the points in the working areas never lie on smooth curves like those in Figure 1(a). The twisting pattern of lines connecting the points in real profiles can be accounted for not only by traces of multiple dimensions, but also by presence of errors which are discussed in [27]. To detect the individual linearity areas, one should find the intervals of arguments in which near-zero curvatures are continuous. Their deviations from zero will be described by a certain distribution function. Since these deviations are assumed to be random, the linear area curvatures obtained using (15) are expected to obey the normal distribution with a maximum close to zero.

Once the parameters of this Gaussian distribution function have been found, one can determine the full range of curvatures satisfying the linearity conditions by means of the three-sigma rule. However, the curvature range in which fitting by the Gaussian function is valid is inherently unknown. Furthermore, the normal distribution approximation is known not to be always justified in statistical investigations, and statistical samplings require special tests for normality. Therefore, the Gaussian fittings are performed over various curvature ranges (from ±0.1 to ±15 with step 0.1). In each step, the 95% probability of the normal distribution applicability is probed using the Shapiro-Wilk test and D'Agostino's K-squared test ([37] and references therein) realized in Matlab codes. Only those distributions are used for finding the zero-curvature scattering which satisfy both tests for normality.

After each step of the validated zero-curvature range determination, the slopes of linear sections in the working areas of the log-log plots are found and accumulated. A plot section is supposed to be linear if the curvatures in this section are within the found range of the zero-curvature scattering. The linear sections are separated from each other by the points corresponding to the curvatures outside this range. Linear sections of the correlation integral and hypersphere-counting plots must include, at least, two zero-curvature points.

These slopes in arrays are cumulated in groups (clusters). The clusters are separated from each other by fairly big gaps. Because there is an uncertainty in finding the fractal dimensions, each of the dimensions is assumed to lie within a cluster. The uncertainty of locating the dimension is simplistically equated to the standard deviation in the group of slopes. Thus, the task of finding the dimension spectrum is reduced to determination of the optimum number of the slope clusters, the mean values and the standard deviations in each of them.

4.2. Discrimination of Slope Clusters in Multi-attractor Data

Dissection of set of points into groups is not a trivial task in mathematical sense. This is the matter of a special part of mathematical statistics called the cluster analysis. In this work, a particular technique of the cluster analysis, termed the partitioning method, is exploited [38]. The standard algorithm of this method, called the k-means algorithm, attempts to minimize the within-cluster sum of squares:

$$\sum_{i=1}^{n_c} \sum_{x_j \in S_i} \left\| x_j - \mu_i \right\|^2 \tag{16}$$

where $\{S_1, S_2, ..., S_{n_c}\}$ is the set of mutually exclusive spherical clusters, μ_i is the mean, or centre, of points x_j in the S_i cluster.

The algorithm tries random starting points and eventually converges at local minima of the sum of squared Euclidean distances. There is no guarantee, however, that the found minimum is global. Another disadvantage of the algorithm is that one has to assign the number of clusters in advance.

Detecting the global minimum of (16) can be secured by repeatedly applying the k-means algorithm to the arrays of attractor dimensions when the number of slope clusters has been predefined. A minimum of the residual sum of squares found among all the trials is taken as the global minimum.

In this work, the k-means algorithm, as a built-in function of Matlab 7, is applied 300 times to each of the dimension arrays. After the minimum of the squared distances has been found, coordinates of the centres in this trial represent mean attractor dimensions.

Finding the optimum number of slope clusters is less straightforward. Consider a model non-uniform array of points in a line, as illustrated in Figure 2. Let a cluster be defined as a group of points comparable with the largest space between two adjacent points in the array. Four clusters are intuitively discernible in Figure 2. The four clusters, by the above definition, would have remained even if a few points had been removed from any of them. Indeed, in this case the gaps in each group are smaller than those separating the clusters. Exploiting the hierarchical clustering terminology, the clusters in this work are defined to be located on one level below the hierarchical top. In general, there is no clear delimitation which size of the clusters should be regarded as that comparable with the largest space. Consequently, the number of clusters defined in the above manner becomes indefinite. The solution to this issue will be sought using the global minimum of the within-cluster sum $\Upsilon_{\min}$ of absolute distances from the centres.

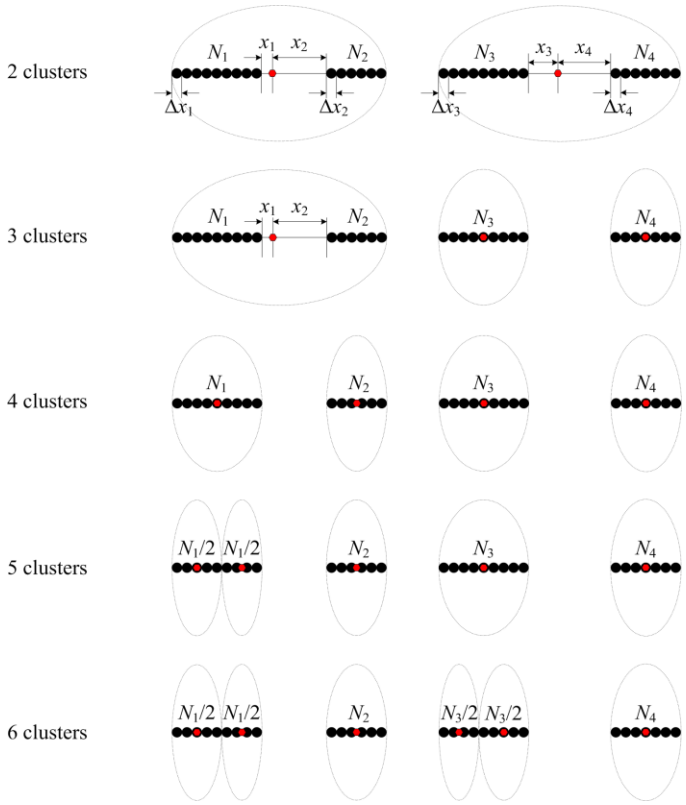

Figure 2. Successive Clustering Applied to the Groups of Points (see the text)

Assume that the location of each cluster centre in the global minimum of (16) is known. In Figure 2 the centres are marked as the coral hexagons. An example of consecutive partitioning in clusters is shown in this figure, with the preset number of clusters successively increasing by unity from the top downwards. The resulting clusters are encircled with dotted lines. The sum of the distances for the two clusters in the uppermost part of Figure 2 is

$$\Upsilon_2 = \sum_{j=1}^{4}\left(x_j + \Delta x_j \sum_{i=1}^{N_j} \frac{i}{N_j}\right) = \sum_{j=1}^{4}\left[x_j + \Delta x_j \left(N_j + 1\right)/2\right], \tag{17}$$

the sum of the distances in the three clusters in the next row of Fig. 2 is

$$\begin{aligned} \Upsilon_3 &= \sum\nolimits_{j=1,2} 2\Delta x_j \sum_{i=1}^{N_j} \frac{i}{N_j/2} + \sum\nolimits_{j=3,4}\left(x_j + \Delta x_j \sum_{i=1}^{N_j} \frac{i}{N_j}\right) \\ &= \sum\nolimits_{j=1,2} \Delta x_j \left(1 + N_j/2\right) + \sum\nolimits_{j=3,4}\left[x_j + \Delta x_j \left(N_j + 1\right)/2\right], \end{aligned} \tag{18}$$

and the sum of the distances in the four clusters one row lower is

$$\Upsilon_4 = \sum_{j=1}^{4} 2\Delta x_j \sum_{i=1}^{N_j} \frac{i}{N_j/2} = \sum_{j=1}^{4} \Delta x_j \left(1 + N_j/2\right) \tag{19}$$

where N_j and Δx_j are, respectively, the number of points and the distance falling on one point in jth cluster.

On the assumptions that the sum of the distances is determined mainly by the large spaces x_j between the dense groups of points and these groups are spaced equally, the difference of (18) and (17) is

$$\Upsilon_3 - \Upsilon_2 = -\sum_{j=1,2}\left(x_j - \Delta x_j/2\right) \approx -\Upsilon_2/2 \tag{20}$$

and the difference between (19) and (17) is

$$\Upsilon_4 - \Upsilon_2 = -\sum_{j=1}^{4}\left(x_j - \Delta x_j/2\right) \approx -\Upsilon_2. \tag{21}$$

One can generalize (20) and (21) as

$$\Upsilon_{a+\Delta n_c} - \Upsilon_a \approx -\Delta n_c\, \Upsilon_a/2. \tag{22}$$

Letting Δn_c approach zero, the separation of variables in (22) and integration yields

$$\ln \Upsilon_a \approx C_1 - n_c/2 \tag{23}$$

where C_1 is the integration constant. Thus, Υ_a decreases exponentially with n_c.

Consider now the sum of distances from the centres of clusters when no large spaces are left within the clusters. From this point on, the partitioning into clusters has to be carried out inside the dense groups of points. This situation is presented in the two lowermost rows in Figure 2. In this case, increasing the number of clusters will yield splitting of the dense groups of points one after another into two equal clusters. Then, the sum of the distances in the five clusters is

$$\Upsilon_5 = 4\Delta x_1 \sum_{i=1}^{N_1} \frac{i}{N_1/4} + 2\sum_{j=2}^{4} \Delta x_j \sum_{i=1}^{N_j} \frac{i}{N_j/2} = \Delta x_1\left(2 + N_1/2\right) + \sum_{j=2}^{4} \Delta x_j \left(1 + N_j/2\right) \tag{24}$$

and the sum of the distances in the six clusters is

$$\begin{aligned} \Upsilon_6 &= 4\sum_{j=1,3} \Delta x_j \sum_{i=1}^{N_j} \frac{i}{N_j/4} + 2\sum_{j=2,4} \Delta x_j \sum_{i=1}^{N_j} \frac{i}{N_j/2} \\ &= \sum_{j=1,3} \Delta x_j \left(2 + N_j/2\right) + \sum_{j=2,4} \Delta x_j \left(1 + N_j/2\right). \end{aligned} \tag{25}$$

The differences between the sums (24), (25) and (19) are

$$\Upsilon_5 - \Upsilon_4 = \Delta x_1 \tag{26}$$

and

$$\Upsilon_6 - \Upsilon_4 = \Delta x_1 + \Delta x_3. \tag{27}$$

In general, on the assumption that every point in each cluster occupies equal space Δx, it follows from (26), (27), and (19) that

$$\Upsilon_{b+\Delta n} - \Upsilon_b \approx \Delta n_c\, \Delta x = \Delta n_c \Upsilon_b \Big/ \left(4 + \tfrac{1}{2}\sum_{j=1}^{4} N_j\right) \tag{28}$$

where b and $b+\Delta n_c$ are the numbers of clusters comprised only of the dense groups of points. Passing on to infinitely small increments, the integration of (28) after the separation of variables results in

$$\ln \Upsilon_b \approx C_2 + k_b n_c \tag{29}$$

where C_2 is the integration constant and $k_b = 1 \Big/ \left(4 + \sum_{j=1}^{4} N_j\right)$.

It follows from (29) that Υ_b increases exponentially with the number of clusters. But because the total number of points can be rather high, k_b is very small and Υ_b is close to being constant. The exponential dependences (23) and (29) of the minimum sum of distances on the number of clusters are the two extreme cases. In fact, the exponential factor can vary from –1/2 or less to k_b as one takes account of increasingly finer levels of spacing between the points.

It is now possible to answer the question which the optimum number of clusters in the array of slopes is. It is the nearest integer to the abscissa of the intersection point of two best successive linear fits in the area of the small values of n_c, when $\ln \Upsilon_{\min}$ is plotted against n_c. There is a bend of the fit slopes around certain n_c. Algorithmically, this point is found in the following way. Consider the linear correlation of $\ln \Upsilon_{\min}$ and n_c. When n_c varies in the range from 2 to i and from i to $n_{c,\text{end}}$ (i is in the range from 3 to $n_{c,\text{end}}$–1), two corresponding correlation coefficients and their product can be calculated. The variation of i yields an array of products of the correlation coefficients in which a maximum is found. The argument n_c corresponding to the maximum product is considered as the borderline for applying the two linear fits on both sides from it. The integer nearest to the intersection point of these fits is the optimum number of clusters.

Summing up, the proposed method provides a fairly reliable estimate of number of attractors and their dimensions in a certain radiometric signal. Like any time-delay phase space reconstruction procedure, it has certain restrictions [27]. In particular, the method can yield distorted or spurious dimensions if a) the initial time series has insufficient number of data; b) there exists lacunarity in the phase space structure of the fractals or a high level of Gaussian noise in the signal; c) the reconstructed vectors are correlated to each other. However, the influence of these errors is smoothed away in the method owing to a) the accumulation of slopes; b) detection of curvature scattering limits; c) statistical averaging of the slopes within a cluster.

In general, the above-mentioned errors can be still more reduced using the minimum mutual information method in determination of time delays [29] and utilizing more extensive data series.

5. Experimentation and Data-processing Procedure Implementation

For our experimentations, a variant [15] of the Dicke radiometer is used. It is designed for 1.88 GHz with the input frequency bandwidth around 100 MHz. The sensitivity announced by the manufacturer is about 0.05 K for $\Delta\tau$=0.1 s. The device is placed in a thermostat with an appropriate temperature to avoid the slow thermal drift of its parameters. The signal is collected by an 8-element microstrip antenna with VSWR≈1.05-1.1 in the mentioned frequency band. The radiometer temperature 36 ℃ is maintained by a thermostat during all the measurements.

The deterministic noise sources of the radiometer may include the high-frequency switches, the nonlinearity of receivers, the A/D convertors, the mismatch of microwave components and antennas, the non-ideal grounding of all equipment, etc.

The following measurements are performed. Eleven students and co-workers from our group (Moscow State Institute of Electronics and Mathematics–Technical University, Laboratory of Bioelectromagnetism), marked as D, G, D1, G1, I1, I, L, M, S, U, and V were chosen for the measurements of their EM radiation. The signals are taken during 1 minute from the chest and head areas of the individuals placed at 3-m distance from the antenna. Additionally, a part of the power is taken by this antenna from the surrounding space due to the antenna's wide main lobe and side lobes. The integration of an analog signal from the radiometer is digitized by an embedded 12-bit A/D converter with the time step Δt=0.495 s, and the data accumulation is restricted to N=121 readings for each sampling. In addition to the signals from the individuals, the noise from a 50-Ohm load and the signal from the environment are registered for the comparison purpose. All the signals have approximately the same level, and they are in the linear zone of the radiometer, which is confirmed by the manufacturer.

The integrated output signal is further processed by means of the state space reconstruction algorithm described in Section 4. For comparison, both the correlation dimensions and the Method-2 Hausdorff dimensions are calculated. The Method-1 of the hypersphere-counting appears unworkable in this case because of slow convergence due to the small number of samples.

The time of first zero of autocorrelation function is adopted as the time delay in processing all the data sets except four cases (persons G1, I1, U, and background noise). The decorrelation time in these cases is too long for processing at high embedding dimensions so that the higher-order dimensions can be overlooked. The time delay for these data sets is calculated from the period corresponding to the most pronounced peak in the Fourier spectra of the signals. Because of the decorrelation time limitation, the data sets are processed for m varying from 2 to 21 for all the individual signals except two ones (G and M) which displayed moderately long decorrelation times (over 3 s). The phase space of these two time series can be reconstructed only up to the embedding dimension 17.

An example of finding slopes for the person S data at m=15 is shown in Figure 3. The linear areas are marked with uppercase Latin letters (in the correlation integral plot) or lowercase Greek letters (in the hypersphere-counting plot) and are associated with certain slope values. The curvature fit range [–0.5;+0.5] in Fig. 3(a) yields the linearity curvature range [–0.66;+0.56] (dashed lines), and the local slopes are 8.15 (A), 7.51 (B), 7.00 (C). The curvature fit range [–0.6;+0.6] in Fig. 3(b) results in the linearity range [–1.11;+1.28] (dashed lines) and the local slopes 4.03 (α), 9.91 (β). Another curvature fit range in this figure, [–1.5;+1.5], yields the linearity range [–2.00;+2.91] (dash-dotted lines) and the local slopes 1.10 (γ), 3.33 (δ), 4.03 (ζ), 2.39 (η), 9.91 (θ).

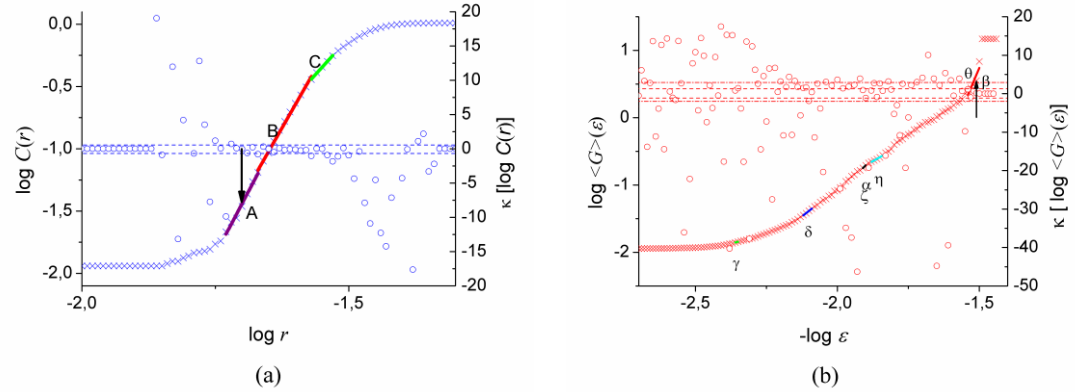

Figure 3. Correlation Integral Plot (a) and hypersphere-counting; (b) plot in logarithmic scales (left axes) as blue and red crosses, respectively (the person S data set, *m*=15). The corresponding curvatures (right axes) are shown as blue and red circles. The arrows denote the onset of linearity for a single fractal dimension. The letters in the plots denote local slopes. The horizontal lines demarcate the curvature boundaries within which plot segments are considered as linear

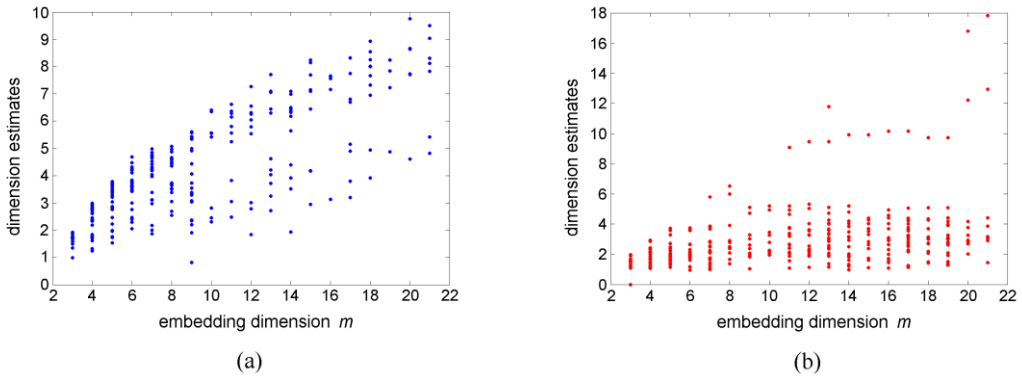

Figure 4. The Slopes of the Correlation Integral Plots (a) and Hypersphere-Counting Plots (b) vs. the Embedding Dimensions (the person S data set)

The results of the entire procedure applied to the person S data set are plotted in Figure 4 against the embedding dimension. One can clearly see saturation of both the correlation dimensions (Figure 4(a)) and the Hausdorff dimensions (Figure 4(b)) below 6. The Hausdorff dimensions in this range are poorly resolved, however. The correlation dimensions have poor resolution above 6 and below 10. No dimensions above 10 have been reliably detected in all the correlation dimension plots for all the data sets.

One sees at least one well-resolved dimension in the Hausdorff dimension plot. This dimension is around 10. The uppermost points in this plot may be related to the white noise in the data. In fact, better resolution of higher dimensions in the Hausdorff dimension plots is observed in processing all the data sets. Thus, as a very favorable result, use of these graphs enables detecting the higher attractor dimensions which are poorly resolved or invisible in the correlation dimension plots. As shown below, it is

higher dimensions that allow distinguishing the background noise and matched load signals from those generated by human body.

The saturation of the attractor dimensions appears to set in approximately in the last third of this embedding dimension range. Consequently, it is the interval in which the observed dimensional estimates can be statistically processed. The slope values are accumulated in the embedding dimension range (14;17) for G and M data sets and (15;21) for the others.

After the arrays of slopes have been accumulated, the partition of the slopes into clusters (Section 4.2) is implemented. The procedure of finding the optimum number of the dimension clusters for the person S data set is exemplified in Figure 5 which shows the logarithm of the global minimum sum of the distances from the centres of clusters vs. number of clusters. Obviously, there is a sharp bend in slopes of fitting lines around n_c=9. Rounding of the abscissas of the intersection points yields nine clusters for both the correlation dimension and the Hausdorff dimension.

It is worth mentioning that the slopes of the fit lines at smaller n_c in Figure 5 are indeed close to the theoretically predicted value –1/2. The slope is –0.49 for the array of the correlation dimensions and –0.55 for that of the Hausdorff dimensions. This is a good corroboration of the assumptions of the dense and nearly uniform filling of the clusters.

Because the assignment of each slope to a certain cluster at the global minimum of ϒ has been stored, one can use it in calculation of the average dimension and its standard deviation in each cluster. The overall dimension patterns thus found are shown and discussed in Section 6.

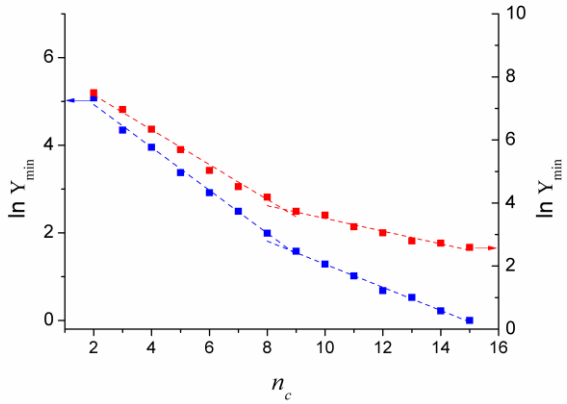

Figure 5. Global minimum sums of distances from cluster centres vs. the number of clusters, as found for the correlation dimension (blue squares) and Hausdorff dimension (red squares) arrays for the person S data set. The dashed lines represent two best linear fits for the successive sum values

6. Results and Discussion

The above data-processing procedure has allowed calculating the attractor dimension spectra from the slopes clustering. Each dimension in the spectrum lies within a certain interval specified by the standard deviation found for a particular group of slopes.

The mean values and spans of all the revealed clusters are shown in Figure 6. The number of clusters for each kind of the dimensions varies from 3 to 10. Because of the method restrictions mentioned above, the slope spans like those in Figure 6 may not

quite accurately reproduce the location of specific attractors in the total pattern. Moreover, the standard deviation may not be an adequate measure to estimate the dimension uncertainty with high probability. However, the method benefits minimize the effects of these errors. The error due to the periodicity might be neglected because no pronounced peaks have been observed in the Fourier spectra of the signals. The analysis of the results plotted in Figure 6 shows that 34 of 81 (42%) intervals in the correlation dimension plot do not intersect with the corresponding Hausdorff dimension intervals. On the other hand, 37 of 77 (48%) intervals in the Hausdorff dimension chart have no correspondence in the correlation dimension results. In the case of the Hausdorff dimensions, most of these intervals fall on the upper part of the chart. Nonetheless, these dimensions unconfirmed by the alternative estimation cannot be rejected for two possible reasons. The first reason is that their area of existence can be narrow ($r \sim r_0$) and they can be masked with overlapping dimensions (see (12)). Another reason is the formation of very prolate spectra of generalized dimensions [27, 34, 35]. The joint pattern from superposition of the correlation dimensions and the Hausdorff dimensions is demonstrated in Figure 7.

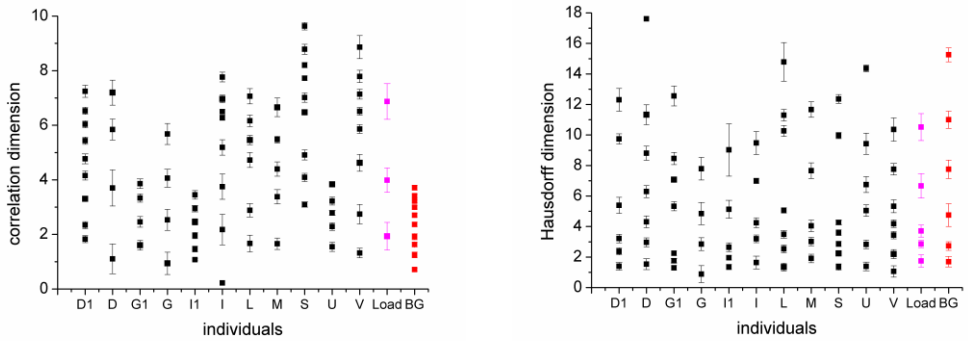

Figure 6. The Correlation Dimensions (a) and the Hausdorff Dimensions; (b) of Multi-attractors in Microwave Signals of Several Individuals, Matched Load, and Background EM Noise

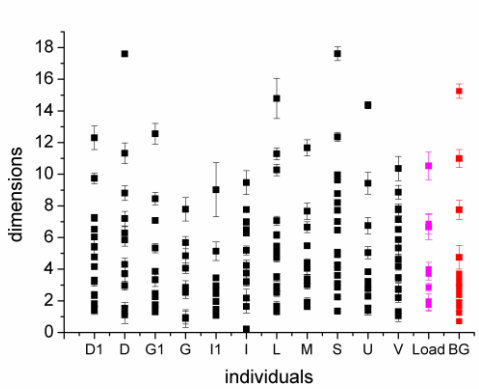

Figure 7. Superposition of the Spectra of Both Dimensions from Figure 6

Poorly resolved low-dimensional attractors in the signals of individuals may originate from the receiver's own attractors and the induced EM noise from other

equipment (Load and BG in Figures 6, 7). Thus, the human attractors with dimensions up to about 5.5, if they exist, cannot be discerned by this method. Some of the high-dimensional attractors (5.86–8.36, 9.64–11.56, and 14.80–15.71) can be ascribed to the background noise and the instrument, too. There are the empty spaces (8.36–9.64 and 11.56–14.80) in the combined dimension spectra of the background noise and matched load. One can notice that some of the dimension spans of certain individuals fall into these "windows". In particular, the lower space contains the dimension intervals of persons S and V and in the higher "window" one can find the dimension intervals of the persons S, D1, G1, and U. Although all these spans, except for the person U, mutually intersect and, therefore, cannot be used as the personal "fingerprints", one can implement this peculiarity for distinguishing the human-generated signals from those of the hardware and background EM noise. One can speculate that these attractors correlate with human body tremor, heart beating, or even correspond to similar attractors registered in the normal state of human brain activity. An alternative point of view on the origin of fractals in the signals involves the projective approach. In fact, the antenna collects the EM power from a larger area than a human body torso, and these spatiotemporal signals are converted into time-dependent signals processed by noisy hardware. This projection may result in the fractal-like time dependence [21,[39].

Because the range of embedding dimensions covered in this work does not exceed 21, it is worthwhile to mention that the fractal dimensions above ten may not attain saturation, according to the Takens suggestion (11). Thus, the actual dimension values of higher-order attractors in the signals are still disputable, and further research is required to reliably establish the origins of these attractors.

The proposed method opens up a possibility of the hardware noise filtering and RFI mitigation in the human radiation signal series. The most straightforward solution of this problem is the removal of the signals constituting those reconstructed state-space vectors which make the largest contribution to the emergence of the dimensions specific for the matched load and background noise spectra. This procedure is supposed to be the trial-and-error technique, and it is expected to consume considerable amounts of time. Therefore, there is a definite need for its optimization and other approaches to the state space refinement are highly desirable.

Unfortunately, the data obtained do not allow making any unambiguous conclusion on possibility of using the described method to detect the human presence in real conditions, since the combined dimension spectra of only five of eleven persons appear distinguishable from those of the background radiation and hardware noise. To prove or disprove this possibility, more experiments are needed. In particular, they should involve longer expositions of individuals to obtain more extensive data series.

7. Conclusions

In this paper, the time-domain characterization of a 1.81-GHz microwave radiometer has been performed. To obtain the reliable data, different sources of thermal microwave radiation have been used, including radiation from eleven individuals. The interference caused by non-ideal design of the radiometer and background EM radiation has been studied using two state-space reconstruction algorithms which allow detection of the deterministic chaos in the noise-like signals.

An original procedure of finding the Hausdorff dimension has been proposed in this work. In contrast to the well-known box-counting method, it is based on averaging the number of unique integer parts of ratios between vector differences and the size parameter. The idea of applying the cluster analysis to the scattered slopes, as a method

for extracting the separate average dimensions, has been implemented in the study by means of the theoretically predicted and computationally verified concept of the optimal number of slope clusters.

Multi-attractors have been found in the signals coming from the individuals, load, and background noise. Their dimensions have been calculated and compared with each other. It is valid to assign most of the attractors to the hardware and EM noise in the laboratory. However, several higher-order dimensions detected in the signals of the individuals have been found beyond the dimension spans of the hardware and background radiation, and the future experimentation has been suggested to explore the origin of these attractors.

References

[1] F. T. Ulaby, R. K. Moore and A. K. Fung, "Microwave Remote Sensing Active and Passive", Addison-Wesley Publishing, Reading MA, vol. 1-3, **(1981)**.
[2] E. A. Sharkov, "Passive Microwave Remote Sensing of the Earth: Physical Foundations", Springer, Berlin, and Praxis, Chichester UK, **(2003)**.
[3] N. A. Armand and V. M. Polyakov, "Radiowave Propagation and Remote Sensing of the Environment", CRC, Boca Raton FL, **(2004)**.
[4] N. Skou and D. Le Vine, "Microwave Radiometer Systems: Design and Analysis", Artech House, Norwood MA, **(2006)**.
[5] Y. B. Zel'dovich and I. D. Novikov, "Relativistic Astrophysics: The Structure and Evolution of the Universe", The University of Chicago Press, Chicago, vol. 2, **(1983)**, pp. 124.
[6] N. Mandolesi, C. Burigana, A. Gruppuso, P. Procopio and S. Ricciardi, Proc. Int. Astron. Union, vol. 6, **(2010)**, pp. 267.
[7] E. E. Godik and Y. V. Gulyaev, "Functional imaging of the human body", IEEE Eng. Med. Biol., vol. 10, no. 4, **(1991)**, pp. 21-29.
[8] K. R. Foster and E. A. Cheever, "Microwave radiometry in biomedicine: a reappraisal", Bioelectromagnetics, vol. 13, no. 6, **(1992)**, pp. 567-579.
[9] Ø. Klementsen, Y. Birkelund, S. K. Jacobsen, P. F. Maccarini and P. R. Stauffer, "Design of medical radiometer front-end for improved performance", Progress in Electromagnetics Research PIER B, vol. 27, **(2011)**, pp. 289-306, NIHMSID:297959.
[10] N. P. Asimakis, I. S. Karanasiou, and N. K. Uzunoglu, "Non-Invasive Microwave Radiometric System for Intracranial Applications: A Study Using the Conformal L-Notch Microstrip Patch Antenna", Progress in Electromagnetics Research (PIER), vol. 117, **(2011)**, pp. 83-101, ISSN: 1070-4698, E-ISSN: 1559-8985.
[11] A. Levick, D. Land and J. Hand, "Validation of microwave radiometry for measuring the internal temperature profile of human tissue", Measurement Science Technology, vol. 22, no. 6, 065801 **(2011)**.
[12] E. Heinz, T. May, D. Born, G. Zieger, S. Anders, G. Thorwirth, V. Zakosarenko, M. Schubert, T. Krause, M. Starkloff, A. Krüger, M. Schulz, F. Bauer and H. -G. Meyer, J. Infrared Milli. Teraherz Waves, vol. 31, **(2010)**, pp. 1355.
[13] K. Chen, Y. Zhu, X. Guo, W. Guo and Q. Li, J. Infrared Milli. Terahertz Waves, vol. 31, **(2010)**, pp. 724.
[14] V. I. Gvozdev, V. I. Krivoruchko, G. A. Kouzaev, and S. Yu. Turygin, Meas. Tech., vol. 43, **(2000)**, pp. 270.
[15] G. A. Kouzaev, M. A. Kulevatov, S. Yu. Turygin and A. S. Cherkasov, Meditsinskaya Fizika (Med. Phys.) vol. 5, **(1998)** (In Russian), pp. 70.
[16] R. H. Dicke, "The measurement of thermal radiation at microwave frequencies", Rev. Sci. Instr., vol. 17, **(1946)**, pp. 268-75.
[17] A. Camps and J. M. Tarongi, "RFI Mitigation in Microwave Radiometry Using Wavelets", Algorithms, vol. 2, **(2009)**, pp. 1248-1262.
[18] B. Güner, N. Niamsuwan and J. T. Johnson, "Performance study of a cross-frequency detection algorithm for pulsed sinusoidal RFI in microwave radiometry", IEEE Trans. Geosci Remote Sens., vol. 48, no. 7, **(2010)** July, pp. 2899-2908.
[19] P. Fanise, M. Pardé, M. Zribi, M. Dechambre and C. Caudoux, "Analysis of RFI identification and mitigation in CAROLS radiometer data using a hardware spectrum analyser", Sensors, vol. 11, no. 3, **(2011)**, pp. 3037-3050.
[20] D. V. Land, A. P. Levick and J. W. Hand, "The use of the Allan deviation for the measurement of the noise and drift performance of microwave radiometers", Meas. Sci. Technol., vol. 18, **(2007)**, pp. 1917.
[21] A. A. Potapov, Zhurnal Radioelektroniki (J. Radio Electron.), vol. 1, no. 1, **(2010)** (In Russian).

[22] P. Grassberger and I. Procaccia, ""Measuring the strangeness of strange attractors", Physica D: Nonlinear Phenomena, vol. 9, no. 1-2, **(1983)**, pp. 189–208.
[23] G. A. Kouzaev and E. A. Bedenko, Meditsinskaya Fizika (Med. Phys.), vol. 5, **(1998)** (In Russian)**, pp.** 72.
[24] F. Takens, "Detecting Strange Attractors in Turbulence", in Dynamical Systems and Turbulence, Lecture Notes in Mathematics, vol. 898, by: D. Rand and B. S. Young, (Eds.), Springer-Verlag, Berlin, Germany, **(1981)**, pp. 366-381.
[25] M. B. T. Leok, Acta Phys. Pol. A, vol. 85, **(1994)**, pp. S-27.
[26] A. A. Tsonis, J. B. Elsner and K. P. Georgakakos, "Estimating the Dimension of Weather and Climate Attractors: Important Issues about the Procedure and Interpretation", J. Atmospher. Sci., vol. 50, **(1993)**, pp. 2549–2555.
[27] J. Theiler, "Estimating fractal dimension", J. Opt. Soc. Am. A, vol. 7, **(1990)**, pp. 1055-1070.
[28] L. F. P. Franca and M. A. Savi, "Estimating Attractor Dimension on the Nonlinear Pendulum Time Series", J. Braz. Soc. Mech. Sci., vol. 23, no. 4, **(2001)**, pp. 427-439.
[29] A. M. Fraser and H. L. Swinney, "Independent coordinates for strange attractors from mutual information", Phys. Rev. A, vol. 33, **(1986)**, pp. 1134-1140.
[30] M. J. McGuinness, "A Computation of the Limit capacity of the Lorenz Attractor", Physica D, vol. 16, no. 2, **(1985)**, pp. 265-275.
[31] G. L. Baker and J. P. Gollub, "Chaotic Dynamics: An Introduction", Cambridge University Press, New York **(1996)**.
[32] E. N. Lorenz, "Deterministic Nonperiodic Flow", J. Atmospher. Sci., vol. 20, **(1963)**, pp. 130-141.
[33] J. W. Havstad and C. L. Ehlers, "Attractor Dimension of Nonstationary Dynamical Systems from Small Data Sets", Phys. Rev. A, vol. 39, **(1989)**, pp. 845-853.
[34] T. C. Halsey, M. H. Jensen, L. P. Kadanoff, I. Procaccia and B. I. Shraiman, "Fractal measures and their singularities: the characterization of strange sets", Phys. Rev. A, vol. 33, no. 2, **(1986)**, pp. 1141-1151.
[35] J. A. Glazier and A. Libchaber, "Quasi-periodically and dynamical systems: An Experimentalist's view", IEEE Trans. Circuits Syst., vol. 35, **(1988)**, pp. 790-809.
[36] M. H. Jensen, L. P. Kadanoff, A. Libchaber, I. Procaccia and J. Stavans, "Global Universality at the Onset of Chaos: Results of a Forced Rayleigh Benard experiment", Phys. Rev. Lett., vol. 55, **(1985)**, pp. 2798.
[37] H. C. Thode, "Testing for Normality", Marcel-Dekker, New York, **(2002)**.
[38] G. A. F. Seber, "Multivariate Observations", Wiley, Hoboken NJ, **(2004)**.
[39] G. A. Kouzaev, I. V. U. Zavedenii, Radioelektronika, vol. 1, **(2001)** (In Russian), pp. 53.

Authors

Sergey V. Kapranov received the M.Sc. degree in Chemistry from V. I. Vernadsky Taurida's National University, Simferopol, Ukraine, in 1998. From 2001 to 2002, he was with Technische Universität München, Freising, Germany. From 2003 to 2004, he was with General Physics Institute and Institute of Organoelement Compounds, Russian Academy of Sciences, Moscow, Russia. From 2004 to 2006, he was with National University of Nuclear Energy and Industry, Sevastopol, Ukraine. He is currently a PhD candidate with the Department of Electronics and Telecommunications, Norwegian University of Science and Technology–NTNU, Trondheim, Norway. His research interests include theory of microwave-initiated chemical reactions, nonlinear dynamics of molecular processes, theory of dielectric relaxation in polar supercritical fluids, and interface chemistry of aqueous systems.

Guennadi A. Kouzaev received the M.S. degree from the Pan-Volga State Academy of Telecommunications and Informatics, Samara, Russia, in 1980, in telecommunications, the Ph.D. degree from the Institute of Radioengineering and Electronics, USSR Academy of Sciences, Moscow, in 1986, in physics and mathematics, and the Doctor of Sciences degree from the Moscow State Institute of Electronics and Mathematics (Technical University), Moscow, Russia, in 1997, in microwave techniques and computer engineering. From 1984 to 1989, he was with the Research Institute of Space Instrument Design, Moscow. From 1989 to 2000, he was with the Moscow State Institute of Electronics and Mathematics. In 1993, he became an Associate Professor, in 1999 a full Professor in the Moscow State Institute of

Electronics and Mathematics (Technical University). From 2000 to 2001 he was with Gennum Corp., Burlington, ON, Canada. From 2001 to 2005, he was with McMaster University, Hamilton, ON, Canada. He is currently a full Professor with the Department of Electronics and Telecommunications, Norwegian Technology and Science University-NTNU, Trondheim, Norway. He has authored over 100 publications and inventions and a Springer book on advanced electromagnetism and microwave techniques. His research interests include electromagnetics, microwave techniques, quantum physics, and bioelectromagnetism. Prof. G.A. Kouzaev is a member of the IEEE. He has taken part in many international conferences being in their scientific boards. Prof. G.A. Kouzaev is a Russian Government Prize Winner (1997) and he was awarded by the Soviet Union Prize for Young Scientists in 1990 for his contribution to the theory and design of three-dimensional microwave integrated circuits.

Vladimir V. Tchernyi (Cherny) received the M.Sc. degree from Rostov-on-Don State University, Russia, and the PhD and Dr. Sci. degrees in Radiophysics. He was with Institute of Radio Engineering, General Physics Institute, Russian Academy of Science, and Moscow State University of Instrumentation and Computer Science, Moscow, Russia. He was also with Volgograd State University, Russia, and University of California at Berkeley, USA. He made a research in microelectronics, fiber and integrated optics, medical physics and space physics. He proposed superconductivity of the Saturn rings origin.